

Md Syam Hasan

Department of Mechanical Engineering, University of Wisconsin, Milwaukee, WI 53211 e-mail: mdsyam@uwm.edu

Filip Zemajtis

Department of Materials Science and Engineering, University of Wisconsin, Milwaukee, WI 53211 e-mail: zemaitis@uwm.edu

Michael Nosonovsky¹

Department of Mechanical Engineering, University of Wisconsin, Milwaukee, WI 53211 e-mail: nosonovs@uwm.edu

Konstantin Sobolev

Department of Civil & Environmental Engineering,
University of Wisconsin,
Milwaukee, WI 53211
e-mail: sobolev@uwm.edu

Synthesis of ZnO/TiO₂-Based Hydrophobic Antimicrobial Coatings for Steel and Their Roughness, Wetting, and Tribological Characterization

We synthesized novel TiO₂/ZnO-phosphate (TP/ZP) and polymethyl hydrogen siloxane (PMHS)-based two-layer hydrophobic coatings with potential antimicrobial properties tuned for application on steel substrates. The mathematical method of topological data analysis was applied to surface roughness data. Wetting characterizations showed stable hydrophobic behavior of the two-layer coated samples. Through tribological characterization, we compared the friction behavior of uncoated steel samples and steel samples coated with different coating materials. The coefficient of friction of uncoated base materials (ranging from 0.221 to 0.269) and the two-layer hydrophobic coatings (ranging from 0.234 to 0.273) indicated that the coatings confer hydrophobic properties to the substrates without a notable change in the friction behavior. We observed the correlations between the wetting and friction behaviors and the average roughness of the coated samples. Analysis of the micrographs of the scratched surfaces revealed preliminary information about the durability and abrasion resistance of the coatings. [DOI: 10.1115/1.4053777]

Keywords: tribology, surface roughness, triboinformatics, coefficient of friction, wetting, contact angle, hydrophobic coating, dry friction, friction, interface, nano-tribology, surface roughness and asperities

1 Introduction

The COVID-19 pandemic has encouraged researchers to investigate the spreading of infectious diseases caused by microbes and viruses and to explore novel methods to limit the transmission. Like many other infections, COVID-19 caused by the SARS-CoV-2 coronavirus primarily spreads through airborne respiratory micro-droplets and aerosols [1–3]. Due to the prolonged survival period of the SARS-CoV-2 and its new strains, contaminated surfaces holding virus-bearing droplets are common sources of infection [4]. Available evidence suggests that direct contact with such contaminated surfaces and subsequent touching of mouth, nose, and eye causes the risk of COVID-19 infection [5]. The World Health Organization (WHO), Centers for Disease Control and Prevention (CDC), and other regulatory bodies in healthcare recommend regular cleaning and disinfecting of commonly touched surfaces to limit the transmission [6,7]. Consequently, the synthesis of surface nanocoatings with effective antimicrobial properties can limit the surface-to-human transmission of the SARS-CoV-2. Antibacterial [8-11] and antiviral [12-14] coatings for surfaces have been explored over the years for different applications. Most of the commercially available antimicrobial coatings, for example, silver-based coatings used in medical applications, incorporate complex synthesis, and application processes, make them expensive. Toxic chemicals and poor durability in applications involving surface interactions are other constraints often limiting the application of the existing antimicrobial coatings.

Contributed by the Tribology Division of ASME for publication in the JOURNAL OF TRIBOLOGY. Manuscript received October 27, 2021; final manuscript received January 31, 2022; published online February 28, 2022. Assoc. Editor: Bart Raeymaekers.

An ideal antimicrobial coating should possess effective photocatalytic properties to deactivate harmful pathogens through catalytic decomposition, sustainable hydrophobic properties to repeal the respiratory droplets, and durability to withstand a wide range of surface interactions without exhibiting toxicity. Antimicrobial treatment based on the photocatalytic property of TiO2 has been studied for different applications including sanitation and sterilization [15–18]. TiO₂ nanoparticles embedded on a surface can oxidize and deactivate organic matters and pollutants deposited on it in the presence of sunlight [15]. The antimicrobial and photocatalytic properties of ZnO nanoparticles are also well studied [19-21]. Our developed TiO₂/ZnO-phosphate (TP/ZP)-based surface coatings incorporate hydrophobic and photocatalytic properties to limit the transmission of pathogens. Hydrophobic properties resist the sustenance of respiratory droplets on the surface and the TiO₂ and ZnO nanoparticles work in pathogen deactivation through the release of hydroxyl radicals during photocatalytic reactions.

Mimicking the "Lotus Effect" for synthesizing water repellent superhydrophobic and self-cleaning surfaces is an example of the application of bioinspiration or biomimetics in material science to synthesize materials with desired surface properties. A special hierarchical roughness profile and the presence of a wax coating in lotus leaves are behind the "Lotus Effect" [22]. The extreme water repellence and hydrophobic behavior of a lotus leaf are desired for many practical engineering applications apart from antimicrobial coatings [23,24]. For example, to increase durability and to decrease water and ice-induced damages of roads and pavements, superhydrophobic concrete or asphalt surface can be a promising solution.

There are different surface wetting states or regimes such as the homogeneous (Wenzel) state with the liquid droplet in full contact with the surface and heterogeneous (Cassie) state, with air pockets trapped under the droplets [25]. Wetting is characterized by the water contact angle (CA) between the surface and a water droplet placed on it. Surfaces are called hydrophilic (0 deg \leq CA

¹Corresponding author.

 \leq 90 deg), hydrophobic (90 deg \leq CA \leq 120 deg), "overhydrophobic" (120 deg \leq CA < 150 deg), and superhydrophobic (150 deg \leq CA \leq 180 deg) depending upon their wetting behavior [26]. Low adhesion and low surface free energy are associated with superhydrophobic and hydrophobic surfaces. Biomimetic superhydrophobic surfaces are synthesized by introducing particle or fiber induced micro/nano level roughness along with a low surface energy coating like polydimethylsiloxane (PDMS), polymethyl hydrogen siloxane (PMHS), polyethyl hydrogen siloxane (PESHO), or polytetrafluoroethylene (PTFE) [27].

Multilayer TiO₂-based coatings have been explored for synthesizing hydrophobic and superhydrophobic concrete for transportation applications. The porous and hydrophilic nature of concrete makes the synthesis of superhydrophobic asphalt or concrete surface a challenging task. However, the combination of microor nanosized particles with PESHO or PMHS admixture has been used to successfully synthesize hydrophobic, overhydrophobic, and superhydrophobic concrete and ceramic tile surfaces [26,28,29]. TP-based hydrophilic first layer of the coating binds the photocatalytic TiO₂ micro- and nanoparticles to the surface and incorporates micro- and nanoroughness. The second layer of a low surface energy coating like PMHS is applied on the first layer. Hydrophobic and overhydrophobic states have been achieved for concrete and tile samples using such modification [15,30]. The photocatalytic oxidizing behavior of TiO2 along with the hydrophobic modification can potentially induce robust self-cleaning properties to the substrate [15,26,30]. A systematic surface characterization can reveal novel insights into the hydrophobic behavior of the synthesized surfaces using novel coatings.

Tribological characterization is required to understand the behavior of the surface coatings during interactions with external stimuli in relative motion. The coefficient of friction (COF) between interacting surfaces is the ratio of friction force (F_f) to the normal load (N) that presses the surfaces together [31,32]. In the widely accepted classical theory of friction, Bowden and Tabor [33] suggested that the friction force involves two mutually independent components due to adhesion (F_a) and the deformation of asperities (F_d). Consequently, the COF or μ can be presented by the following equation:

$$\mu = \frac{F_f}{N} = \frac{F_a + F_d}{N} = \frac{F_a}{N} + \frac{F_d}{N} = \mu_a + \mu_d \tag{1}$$

In the equation, μ_a and μ_d denote the COF components for adhesion and deformation, respectively [34,35]. The tribological characterization will reveal how the developed coatings are altering the friction behavior of the surfaces.

In this article, we will document the synthesis of two-layer hydrophobic antimicrobial surface coatings of TP/ZP and polymethyl hydrogen siloxane for steel samples. We will characterize the surface roughness and determine the wetting and tribological properties of the synthesized samples. We further analyze the durability of the developed coatings for tribological applications. Finally, we investigate correlations between surface roughness and corresponding wetting and tribological behavior.

2 Materials and Procedures

2.1 Sample Preparation. In this section, we have discussed the synthesis and application of the coatings in preparing samples for experimental studies.

Two grades of steel, 1018-grade cold-finished carbon steel (CS) and 304 grade and annealed stainless steel (SS), were supplied from Speedy Metals (New Berlin, WI) and were used as substrates further referred to as the base material (BM) for the coatings. The BM samples were machined to 1 in. \times 1 in. size coupons, sandblasted and ultrasonically cleaned in an acetone bath. Some of the carbon steel BM samples were then phosphated in a room temperature bath (composed of ZnO 5 g/L; 85% $\rm H_3PO_4$ 11.3 mL/L; NaNO₂ 1 g/L dissolved in $\rm H_2O_{di}$ —all these precursors were purchased

from MilliporeSigma, USA) and referred to as RTP CS. After immersing in the bath for 30 min, the RTP CS samples were rinsed thoroughly with water and dried in air. All three substrates: CS, SS, and RTP CS were further used for coating application and performance analysis.

To synthesize the hydrophilic base layer (first layer of the coating). well-mixed solutions of coating materials S1 and S2 (details in Table 1) were prepared with different compositions of phosphoric acid (H₃PO₄), zinc oxide (ZnO), titanium dioxide (TiO₂), and water. These coating materials were applied to the BMs using spincoating techniques. To assure repeatability, each coating solution was applied on the base metal on a similarly adjusted spin coater. Each time, seven drops of the solution were placed on the surface while spinning at 1500 rpm for the duration of 15 s. The coated BM samples were heat-treated in the oven at 250 °C for 1 h. After heat treatment, the samples were removed from the oven and allowed to cool at room temperature. To synthesize the hydrophobic layer (second layer of the two-layer coatings), 1 wt% PMHS solution (DOW, Midland, MI) dissolved in acetone was used. The second layer was applied on the sintered hydrophilic samples (coated with the first layer) to synthesize the two-layer hydrophobic coatings. The samples were then heat-treated at 150 °C for 15 min and aircooled at room temperature to attain hydrophobic properties. The PMHS-based hydrophobic layer was also applied to the BM samples directly (without the first layer) to synthesize one-layer hydrophobic samples. The schematic diagram of the coating layers on the base material surface is shown in Fig. 1.

The base materials and the synthesized hydrophilic and hydrophobic samples of the abovementioned compositions were further characterized.

2.2 Surface Roughness Characterization. Surface characterization was performed using a scanning electron microscope (SEM) and confocal laser scanning microscope (CLSM). To characterize surface roughness and patterns of the sample surfaces, an Olympus LEXT OSL model-4100 CLSM was used. The samples were placed on the sample stage of the microscope using the joystick eight spots on different locations of each sample and were selected randomly for characterization. The average roughness, R_a , of each sample was reported by averaging the R_a of each measurement for a sample surface. Using the LEXT software, threedimensional images of the surface at 20× magnification were captured by laser scanning. With a resolution of $0.625 \mu m$, the sampling profile length of 80 µm was selected in both x- and y-directions. Besides the image profiles, the surface roughness profiles were recorded in numeric data sets as 128 × 128 matrices and stored in csv files. From each scan, 16,384 data points of the roughness height were received.

Table 1 The formulation of coating materials

Coating material	Wetting behavior	Heat treatment duration (h)	Water/ acid ratio (W/A)	Oxide used	Oxide/ acid ratio (O/A)
Uncoated BM	Hydrophilic	n/a	n/a	n/a	n/a
S1	Hydrophilic	1	6	ZnO	0.4
S1h	Hydrophobic	1.25	6	ZnO	0.4
S2	Hydrophilic	1	10	ZnO: TiO ₂ Ratio of 0.9	1.1
S2h	Hydrophobic	1.25	10	ZnO: TiO ₂ Ratio of 0.9	1.1

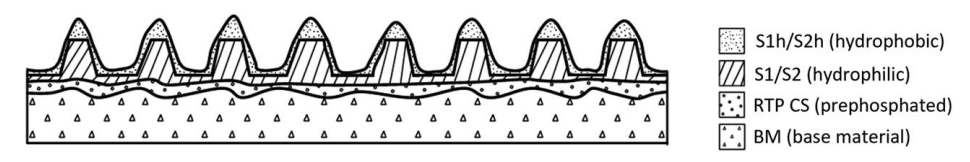


Fig. 1 Schematic diagram of different coating layers on the base material surface

To characterize the overall surface appearance, JEOL JSM-6460L Scanning Electron Microscope was used. Prior to characterization, the specimens were gold/palladium sputtered to improve sample conductivity, reduce surface charging, and increase the quality of overall micrographs using Denton Desk II Sputter Coater. Secondary electrons accelerated to 15 kV were used as a source. Every image was taken on a 45-mm spot size and a working distance of 12 mm.

2.3 Tribological Test Procedure. For tribological characterization, we measured the COF between the samples and the highdensity polyethylene (HDPE) pin using the universal mechanical tester (CETR UMT 2) under dry conditions. Using a metallic pin caused the significant removal of materials from the uncoated and coated samples, and no longer presented the friction behavior of the surfaces (rather presented that of the bulk material). On the other hand, the HDPE pin helped to characterize the friction behavior of the uncoated and coated surfaces consistently as no notable material removal was involved. The standard pin-on-flat reciprocating testing regime was used for the COF measurement, where the samples were slid in a reciprocating motion against the static HDPE pin having a diameter of 6.35 mm. The sample was placed in a sample holder specially designed for holding the 1 in. \times 1 in. samples. Then, it was mounted on the reciprocating base of the tribometer, which is designed to move along the x-axis (horizontally) with the help of a DC motor. The HDPE pin was attached to the upper frame of the suspension of the tribometer, which is connected to the sensor (DFH-50-0767). Using the UMT software, the motion of the sample holder and the suspension was controlled. The tribological test variables (normal load, sliding velocity, and sliding distance) were set by writing a command script in the UMT software.

During the experiment, a constant normal load was maintained by the control unit through a continuous adjustment of the Z carriage movement in the vertical direction. The command script of our tribological test included a preload sequence: 15 N normal load with a slider velocity of 2 mm/s for 30 s and a reciprocating sequence: 15 N normal load with a slider velocity of 0.2 m/s for 120 s. The normal load of 15 N was selected (which is in the recommended range of the DFH-50-0767 sensor) after running the friction tests of the tribo-pairs for different normal loads (5 N, 15 N, 20 N, 25 N, and 30 N) and visually observing the scratch marks on the surface. A stroke length of 10 mm and the corresponding 0.2 m/s sliding velocity, which is in the recommended range, were used in the pin-on-flat reciprocating test. The run-time of the tests was selected fulfilling the requirement of the pin-on-flat reciprocating test.

The DFH sensor detected the frictional force and the normal load continuously during an experiment and transferred the signals to the UMT software. Finally, the software prepared a data sequence file by converting the signals which exhibited the results of the tribological test. In standard pin-on-flat reciprocating tests, the *x*-axis is defined as the axis of sliding and the *z*-axis is defined as the direction of the normal load. We did not intend to have any directionality in the synthesized samples. The tribological tests were repeated four times on different locations (the sample was rotated in the sample holder) of each sample, and the average COF was reported.

2.4 Wetting Test Procedure. To characterize wetting, we measured the water contact angles of the samples using the Rame-Hart 250 goniometer. The device is composed of several components: micro-syringe assembly, sample holder base, a high-speed camera, and a light source (Fig. 2).

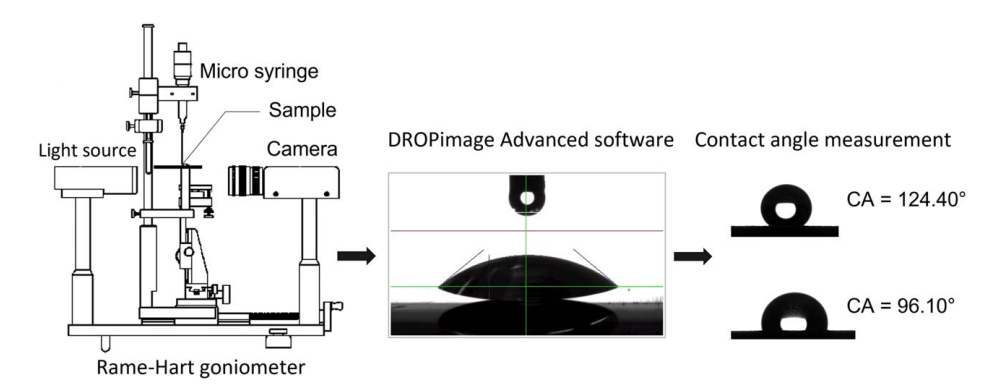


Fig. 2 Measurement of contact angles with a Rame-Hart goniometer

Table 2 Properties of base materials before and after hydrophobic treatment

	Average roughness (μ m)		Coefficient of friction		Contact angle (deg)	
BM	BM	+ PMHS coating	BM	+ PMHS coating	BM	+ PMHS coating
CS RTP CS SS	3.705 2.805 2.907	2.611 2.039 2.071	0.256 ± 0.077 0.269 ± 0.081 0.221 ± 0.063	0.174 ± 0.055 0.155 ± 0.041 0.178 ± 0.045	- - -	$98.37 \deg \pm 0.21 \deg$ $95.65 \deg \pm 1.55 \deg$ $97.30 \deg \pm 1.21 \deg$

Table 3 Properties of the coated hydrophilic and hydrophobic samples

Coating material	ВМ	Average roughness (µm)		Coefficient of friction		Contact angle (deg)	
		Phosphate coating	+ PMHS	Phosphate coating	+ PMHS	Phosphate coating	+ PMHS
S1	CS RTP CS SS	6.473 4.96 5.722	8.805 5.016 6.161	0.193 ± 0.074 0.207 ± 0.055 0.194 ± 0.076	0.273 ± 0.081 0.245 ± 0.069 0.263 ± 0.075	- - -	124.33 deg ± 0.78 deg 111.93 deg ± 3.26 deg 112.68 deg ± 4.01 deg
S2	CS	4.004	7.522	0.233 ± 0.072	0.234 ± 0.076	_	$121.97 \deg \pm 0.86 \deg$

Using the micro-syringe assembly, we placed $4-\mu L$ distilled water (DI) droplets at five different locations on the samples. The images of the droplets were captured by the high-speed camera and were then analyzed by the "DROPIMAGE" software for the CA characterization. "DROPIMAGE" software provided the CA values at each location, which were then averaged and reported as the CA of the samples.

3 Results and Discussion

In this section, we have presented the characterization and experimental results for the uncoated base materials and the coated samples.

3.1 Surface Roughness Characterization. The average roughness, R_a , of the base substrate materials and the coated samples are presented in Tables 2 and 3. The R_a values of the BM samples of CS, RTP CS, and SS were $3.705 \,\mu\text{m}$, $2.805 \,\mu\text{m}$, and $2.907 \,\mu\text{m}$, respectively. The microstructure of the BM surfaces is shown in Fig. 3 that displayed surface appearance prior to the coating application. Both the CS and the SS surfaces were observed to be similarly roughened as a similar surface treatment was used. In the micrograph of the prephosphated carbon steel (RTP CS), due to the phosphating reaction, structures composed of fine zinc and iron phosphate crystals were developed that emerge from the surface (visible at higher magnification placed at the right top corner).

Table 2 shows that the application of the single layer of PMHS on the BM decreased the R_a . In contrast, the single layer of TP/ZP

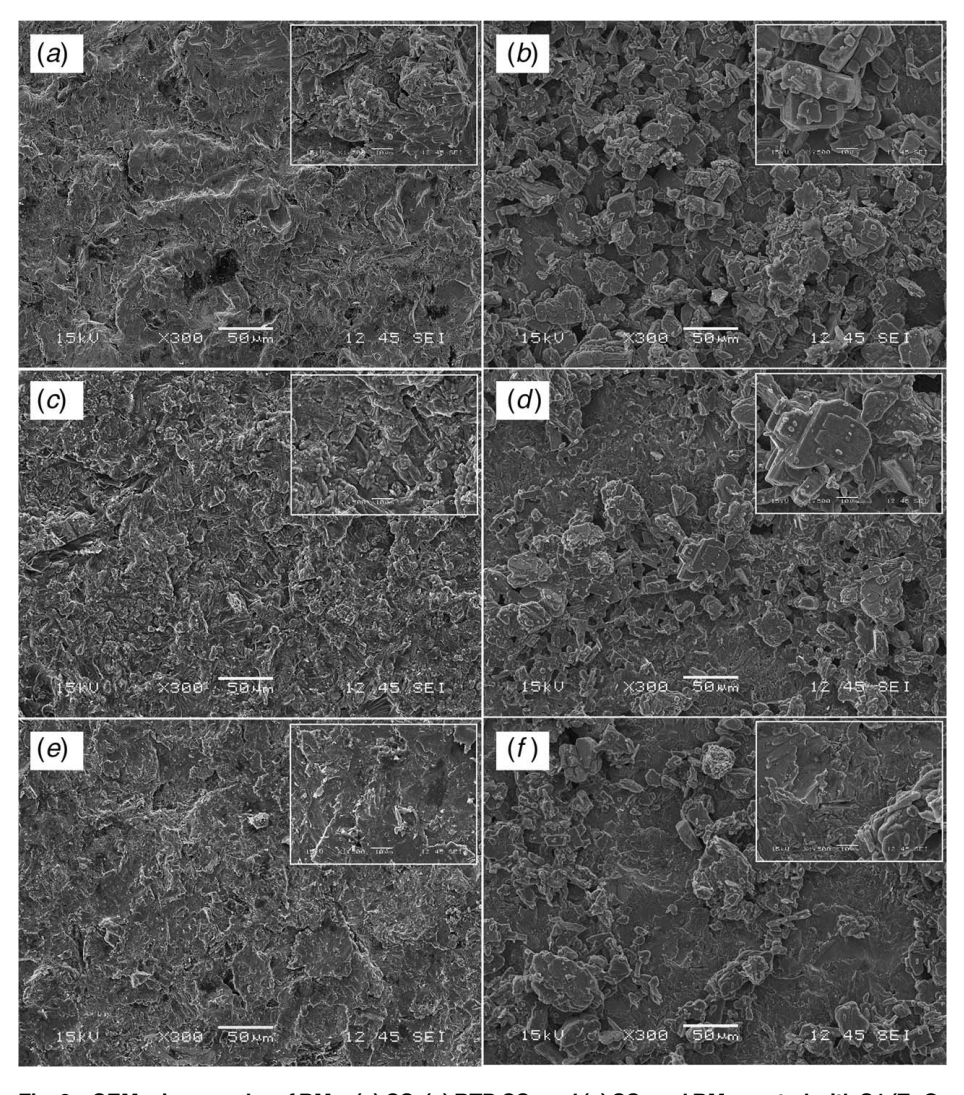


Fig. 3 SEM micrographs of BMs: (a) CS, (c) RTP CS, and (e) SS, and BMs coated with S1 (ZnO-phosphate) coating material: (b) S1 CS, (d) S1 RTP CS, and (f) S1 SS

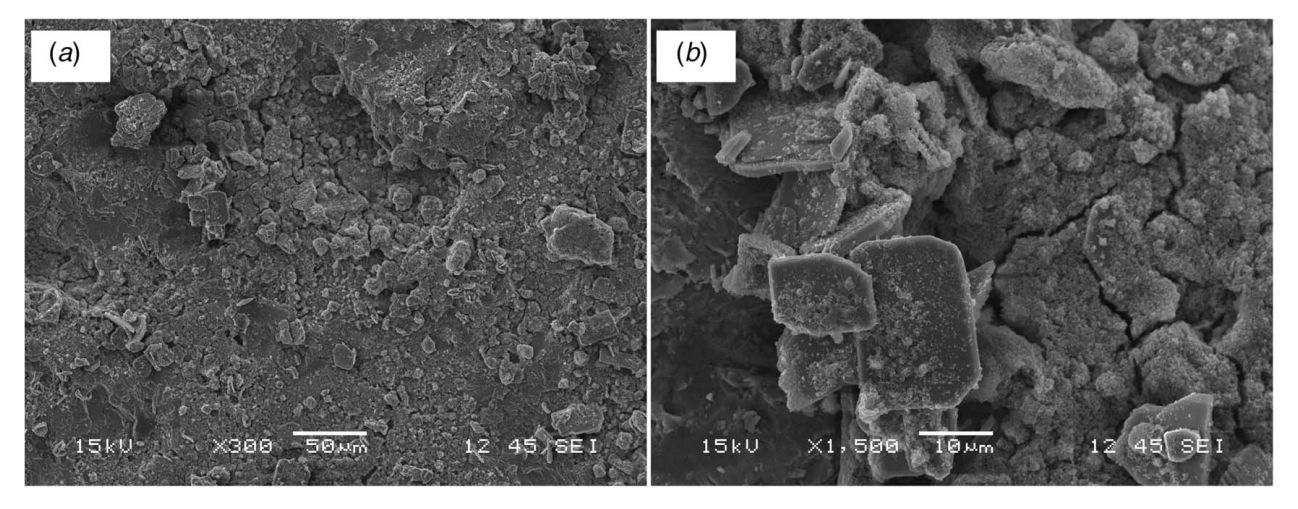


Fig. 4 SEM micrographs of CS base substrate coated with S2 coating material (TP-ZP) at (a) 300x and (b) 1500x magnification

coatings on the BM increased the R_a notably. A further increase in R_a was observed when an additional layer of PMHS was applied over the TP/ZP layer. The R_a values observed for the two-layer coating on the CS, RTP CS, and SS BM samples were $8.805~\mu m$, $5.016~\mu m$, and $6.161~\mu m$, respectively. Among the BM samples, the carbon steel exhibited the maximum R_a of $8.805~\mu m$ when the two-layer coatings were applied on the sample. The micrographs of the surface of the BM samples with the S1(ZP) and S2 (TP-ZP) coating materials were shown in Figs. 3(b), 3(d), 3(f), and 4, respectively.

In the X-ray diffraction (XRD) analysis, for all three substrates coated with the S1 coating material, the presence of crystalline zinc phosphate on the surfaces was confirmed. In the case of the coated carbon steel (S1 CS) and prephosphated carbon steel (S1 RTP CS) samples, the crystal structures were dense and highly developed. In contrast, the coated stainless steel (S1 SS) sample demonstrated lesser attachment of crystals to the surface, thus forming microstructure of lower density compared to S1 CS and S1 RTP CS products. The micrograph of the CS BM coated with the S2 coating material (Fig. 4) exhibited a distinct surface morphology. Crystal structures of zinc phosphate (platelets) protruding through a nano-titania layer were observed.

3.2 Topological Data **Analysis** and Surface Characterization. Here, we have applied the method of surface roughness analysis earlier developed in Ref. [36]. Surface roughness data involve many parameters, which are usually organized in multidimensional space [36]. The reduction of the dimensionality of the data (i.e., the organization of data in subspaces along the surface) is achieved through topological analysis. Topological data analysis helps to identify persistent features over different resolution scales, which represents the true features of the underlying space, unlike random noise and artifacts. Persistent homology involves the computation of topological features: topological invariants, n-dimensional simplicial complex, Betti numbers, etc., at different spatial resolutions. Connected components (H_0) , one-dimensional (1D) holes (H_1) , and higher dimensional voids $(H_2, H_3, \text{ etc.})$ are the major topological invariants observed over varying length scales. The appearance and disappearance of homological invariants or features in different sampling lengths are presented in the persistence diagram. The most persistent topological features are presented by the data points that are located far away from the diagonal. In barcodes, each horizontal bar presents the interval of the feature appearance and disappearance. While shorter bars are representative of random noises, the longer bars present the more persistent topological invariants.

To analyze the surface topology, we considered the surface profile (roughness height) data of the CS BM, CS BM-PMHS, S1

CS, and the two-layer S1 CS-PMHS-coated samples. We presented the persistence homology with persistence diagrams and barcodes in Fig. 5, where the homological invariants were expressed as a function of the resolution length. A sampling length of $80 \, \mu m$ with a resolution of $0.625 \, \mu m$ in both x- and y-directions was considered. For generating the diagrams for surface profile data, we used the standard libraries of PYTHON. The data sets in the form of 128×128 matrices were subdivided into 3×3 submatrices for generating the barcodes [36,37]. First, we generated a filtered simplicial complex from the data points. We considered Vietoris–Rips filtration in the analysis and the maximum dimension of 4 to calculate the persistent homology for the Euclidean distance matrix.

Each of the samples exhibited a distinct topology for the surface profile data at different length scales in Fig. 5. For the uncoated CS BM sample, H_0 , H_1 , and H_2 were the major persistent topological invariants. The first topological invariant, H_0 , which indicated the connected components in topological space, was found persistent over the entire sampling length range. The other persistent invariant, H_1 , corresponding to 1D holes was significant at the resolution length corresponding to the size scale of the profile, approximately in the range of 35–45 μ m. Application of the hydrophobic PMHS layer on the CS BM caused a decrease in average roughness (Table 2). From the persistence diagram and barcodes, it was seen that the higher dimensional void (H_2) is no longer persistent for the CS BM-PMHS sample as the surface is smoothened. For the S1 CS sample, well-developed crystalline structures of ZP were observed on the surface and the average roughness increased notably (Table 3). Due to more complex surface morphology, an additional higher dimensional void (H_3) invariant was found persistent besides H_0 , H_1 , and H_2 from the persistence diagram and barcodes. Longer bars for H_3 in the barcode diagram for the S1 CS sample (Figs. 5(e) and 5(f)) indicated that higher-dimensional voids were more prevalent than those observed in the BM sample. Moreover, this invariant was significant at the resolution length corresponding to the size scale of the profile, approximately in the range of $45-52 \mu m$. For the two-layer S1 CS-PMHS samples, the average roughness increased further. However, the second layer of PMHS covered the ZnO-phosphate crystal structures and made the surface profile more uniform. Consequently, in the persistence diagram and barcodes, the 1D holes (H_1) and the higher dimensional voids (H_2, H_3) were found less persistent than those of the CS BM and the S1 CS samples.

To analyze the roughness data and visualize the patterns in roughness profiles for CS BM, CS BM-PMHS, S1 CS, and the two-layer S1 CS-PMHS hydrophobic samples, we divided the 128×128 matrix of each representative sample's roughness profile into 3×3 square submatrices (3698 units) using a PYTHON program. The average roughness values of these samples were $3.705 \, \mu m$, $2.611 \, \mu m$, $6.473 \, \mu m$, and $8.805 \, \mu m$, respectively. To compare the

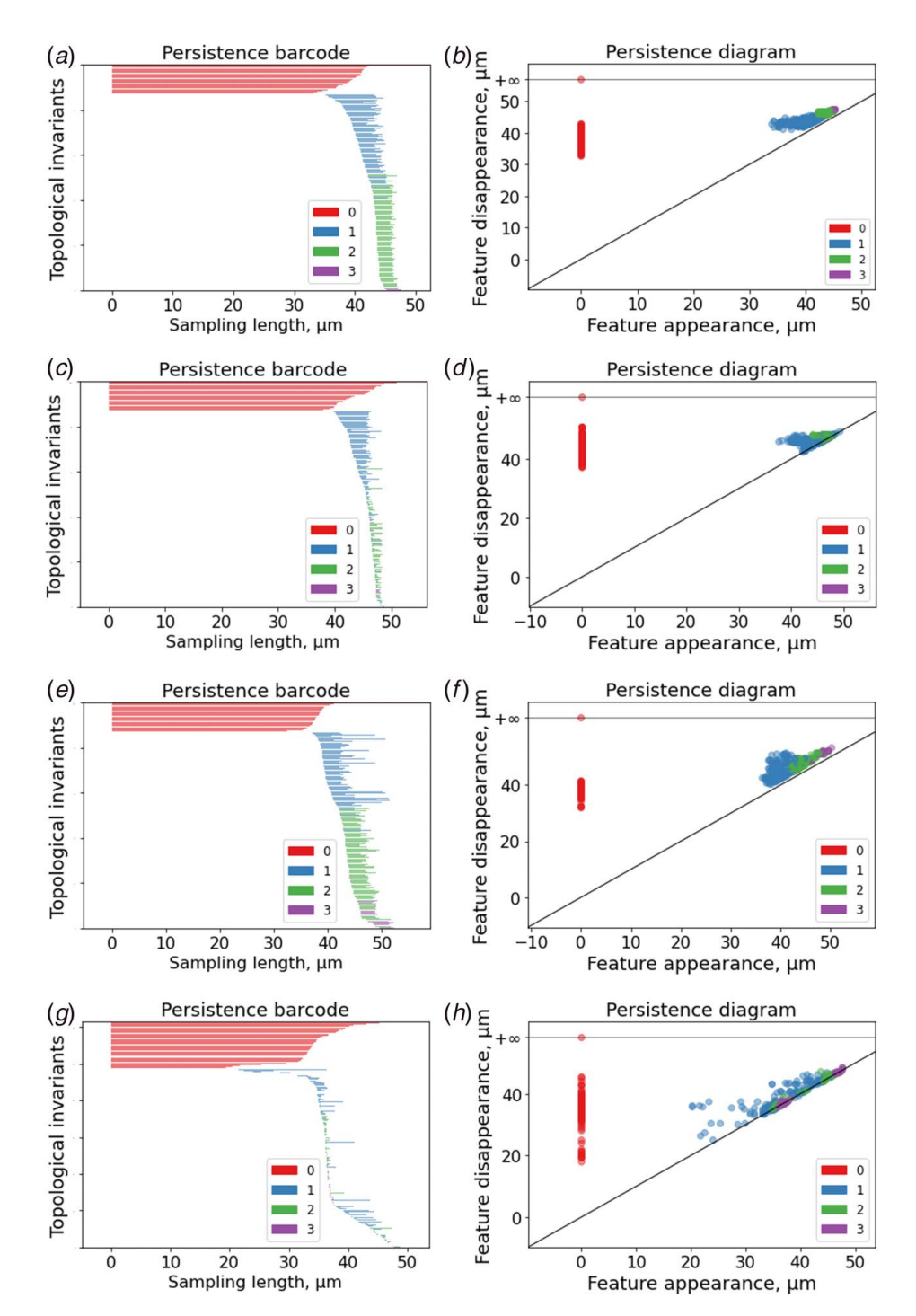


Fig. 5 Persistence diagram and persistence barcodes for the surface roughness of (a) and (b) CS BM, (c) and (d) CS BM-PMHS, (e) and (f) S1 CS, and (g) and (h) two-layer S1 CS-PMHS samples

roughness profiles, we considered the sampling length of $80 \, \mu m$ with the resolution of $0.625 \, \mu m$ in both the horizontal and vertical directions (x- and y-directions) for each sample. The autocorrelation function (ACF) and the distribution of the maximum and minimum roughness heights in cell positions for the submatrices for the above-mentioned samples are shown in Fig. 6. Among the samples, the CS BM had the largest correlation length, β^* (the smallest sampling length at which the ACF dropped to 10% of its original value) along the x-direction ($20.9 \, \mu m$) and the y-direction ($17.5 \, \mu m$). The minimum value of β^* was found for the hydrophobic CS BM-PMHS sample ($8.5 \, \mu m$ along the x-direction and $15.4 \, \mu m$ along the y-direction). The β^* values for the S1 CS

 $(11.9~\mu m)$ and $11.0~\mu m$ along the x- and y-directions) and the two-layer S1 CS-PMHS sample $(18.1~\mu m)$ and $12.5~\mu m$ along the x- and y-directions) were also notably smaller than those of the CS BM. These β^* values indicated that surface profile and patterns in the coated samples were changing more rapidly along the sampling length than observed for the uncoated BM.

For the two-layer S1 CS-PMHS hydrophobic sample, the diagonal cell positions of the 4×4 submatrix: (0,0), (0,2), (2,0), and (2,2) held the most maximum and minimum values of the roughness heights (Fig. 6(g)). The correlation length for the roughness profile was notably greater than the size of the patch of $1.875 \, \mu m$, and the greatest number of maxima and minima was observed at

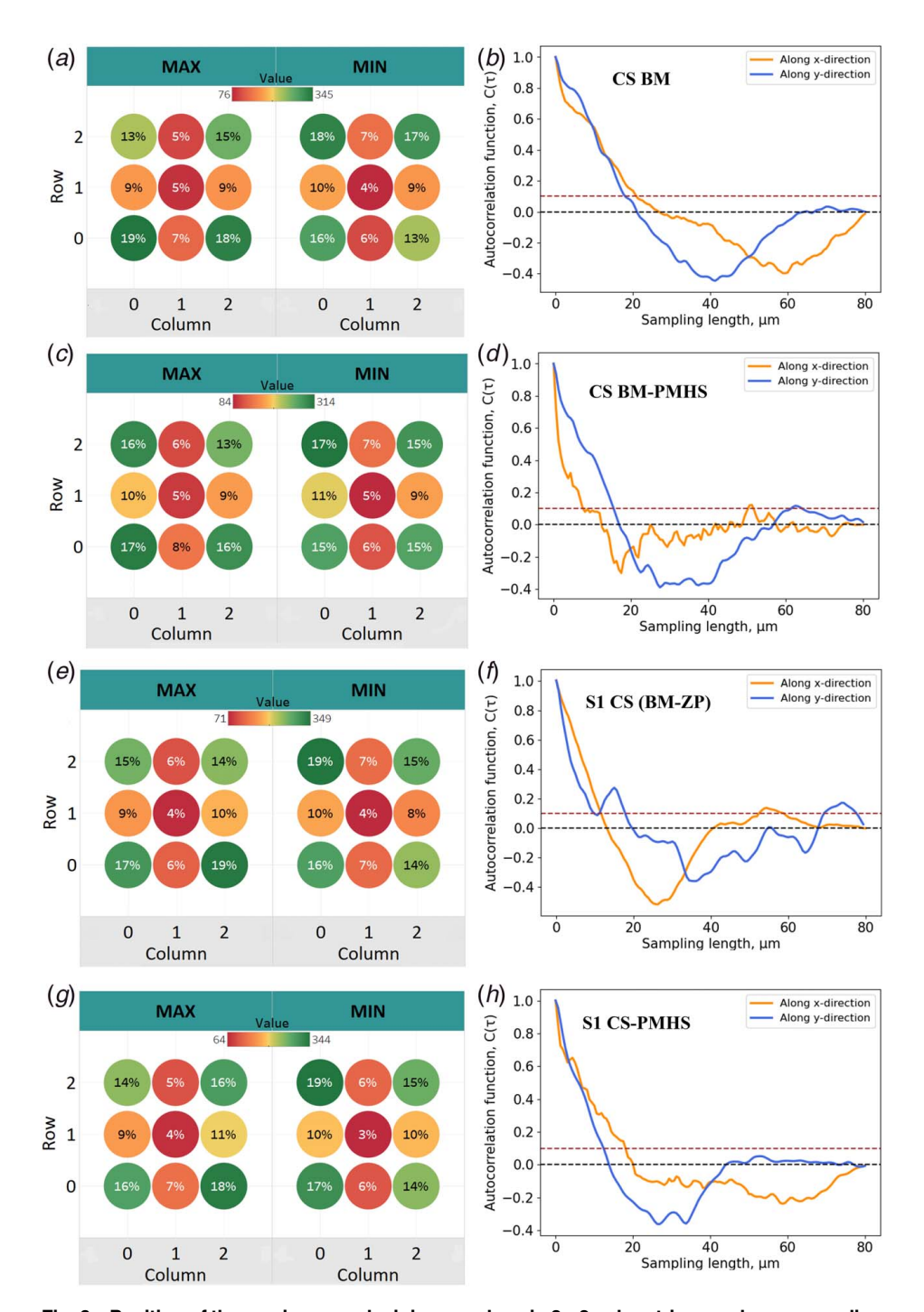


Fig. 6 Position of the maximum and minimum values in 3×3 submatrices and corresponding autocorrelation function for surface profile data for (a) and (b) CS BM, (c) and (d) CS BM-PMHS, (e) and (f) S1 CS (BM-ZP), and (g) and (h) S1 CS-PMHS

the diagonal positions. Moreover, the total percentage of the number of maxima and minima in the positions (0,1), (2,1) was 12% (for maxima) and 12% (for minima), while the total percentage in the positions (1,0), (1,2) was 20% (for maxima) and 20% (for minima). This suggested that the distribution was anisotropic (Fig. 6(g)), where the surface gradients for surface roughness in the *x*-direction were more prevalent than in the *y*-direction. The distribution of the maxima and minima varied among the other samples. However, we observed the anisotropic distribution of roughness in each case in vertical and horizontal directions.

Besides characterizing the surface roughness of the samples using traditional measurement techniques, we studied correlation lengths, analysis of the extreme point location, and persistence diagrams in the data space. Novel insights into the roughness properties were generated by these parameters, which were beyond the scope of the traditional quantitative surface roughness characterizations. From the autocorrelation functions, information on the horizontal size of the microscale roughness details was received. Details about anisotropic microscale features that are not identified by the more traditional roughness parameters were presented by the analysis of the 3×3 submatrices. The persistence diagrams and barcodes presented the details of the scale-dependency of the roughness features.

3.3 Wetting Test. The wetting test results of the samples are presented in Tables 2 and 3. The uncoated BM samples after

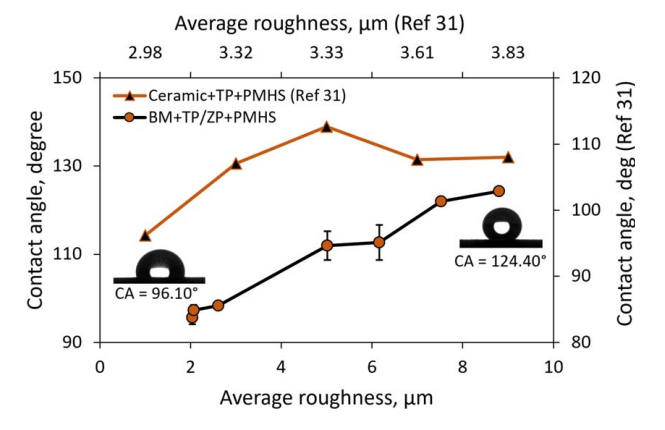


Fig. 7 Contact angle versus average roughness plot of hydrophobic samples

sandblasting and the BM samples coated with S1 and S2 coating materials were hydrophilic in nature without a stable wetting profile. We did not report the CA of those hydrophilic samples. BM samples with the single layer of the PMHS coating exhibited stable wetting profiles with average CAs between 95.65 deg and 98.37 deg. In contrast, the samples coated with the two-layer coatings (S1 or S2 coating material+PMHS) exhibited impressive hydrophobic behavior, where the average CA varied between 111.93 deg and 124.33 deg. We plotted CAs of the hydrophobic samples against average roughness in Fig. 7. We also presented the CAs of ceramic tiles coated with TP and PMHS layers against

the average roughness from our previous study [30]. In each case, the CA increased with an increasing average roughness of the samples, which is consistent with other studies [30,34,38].

BMs coated with a single layer of PMHS had smaller average roughness values among the hydrophobic samples and exhibited smaller CAs. Samples coated with the S1 and S2 coating materials (TP/ZP layer) followed by the PMHS layer had larger average roughness and exhibited larger CAs. Figure 8 shows the micrographs of the samples. The two-layer coating of TP/ZP and the PMHS layers induced the maximum average roughness on the carbon steel BMs. The maximum CA (124.40 deg) was observed for the CS sample coated with the two-layer coating. The micrographs demonstrated that the crystal structures were well-covered by the PMHS layer, which made their appearance more blurred in the micrographs. Among the samples (Fig. 8), the surface of the S1 h CS sample was less blurred by the PMHS layer, which was distributed more evenly as the crystal structures on this substrate were more developed.

3.4 Tribological Tests. We present the tribological test results for the base materials and the coated samples in Tables 2 and 3. We used the COF of the BM samples as references to compare the friction performance of the developed coatings. For the BM samples, the COF ranged between 0.221 ± 0.063 and 0.269 ± 0.081 . For BM samples coated with the single layer of PMHS, a notable reduction in COF was observed (ranging between 0.155 ± 0.041 and 0.178 ± 0.045). As the BM surfaces were modified with the low surface energy coating, the surfaces were smoothened, and the average roughness was reduced. Consequently, lower COF values were observed for the samples.

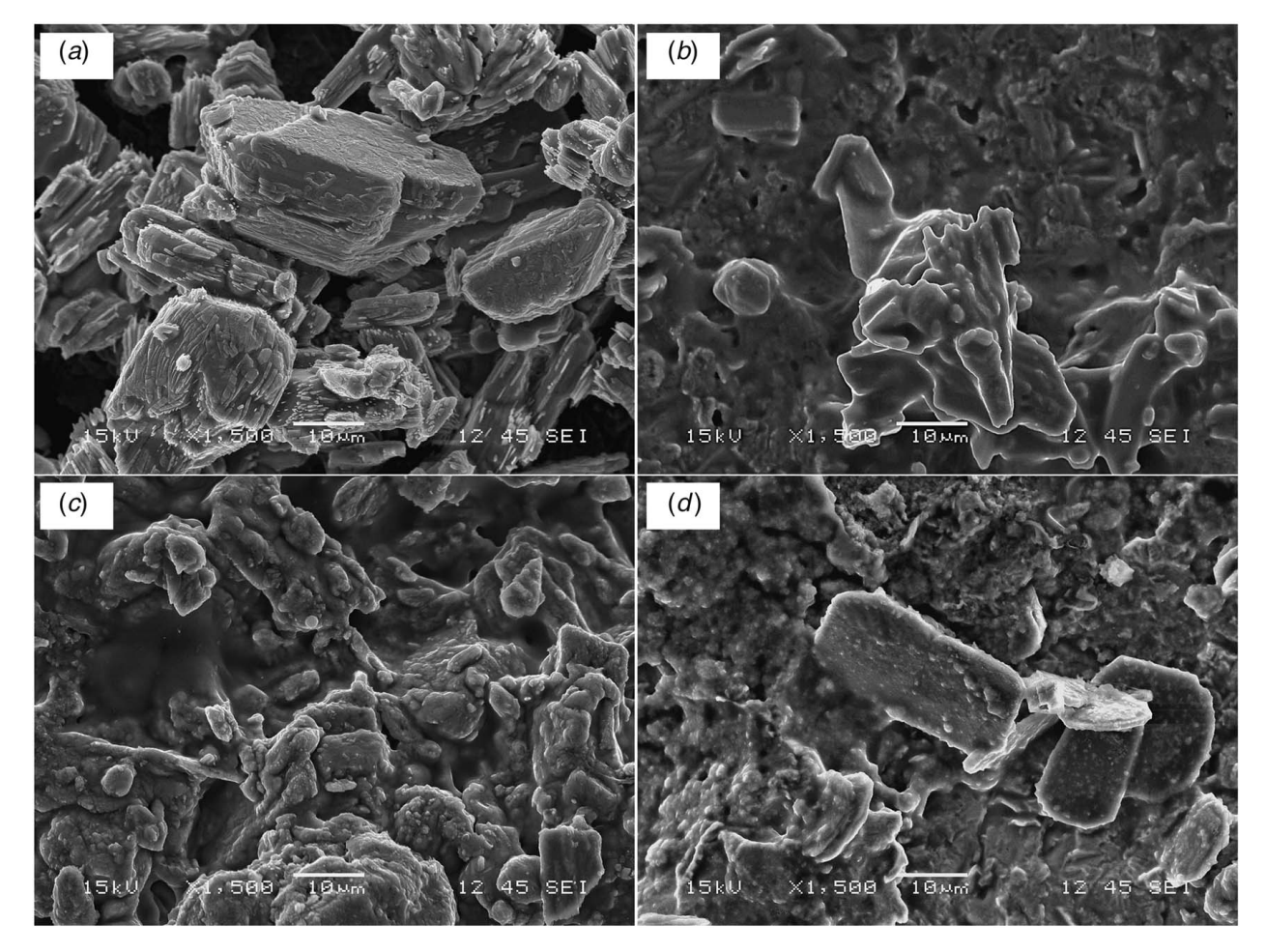


Fig. 8 Micrographs of two-layer (TP/ZP + PMHS) coated samples: (a) S1 h CS, (b) S1 h RTP CS, (c) S1 h SS, and (d) S2 h CS

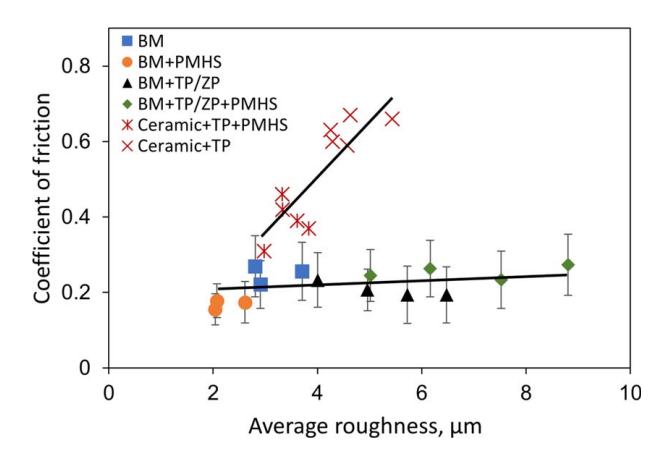


Fig. 9 COF versus average roughness plot for uncoated steel BMs and BMs coated with TP/ZP+PMHS and comparison with COF versus average roughness for ceramic tile samples coated with TP and TP+PMHS (based on Ref. [30])

Base material samples coated with the single-layer S1 (ZP) and S2 (TP-ZP) coating materials also exhibited lower COF than the uncoated BM samples. Ceramic debris generated in a powder form during the tribological testing provided a lubrication effect, which caused the reduction in COF. However, the COF was slightly higher than the PMHS-coated samples. BM samples coated with the two-layer hydrophobic coatings (first layer of the S1 or the S2 coating material followed by a second layer of PMHS) exhibited

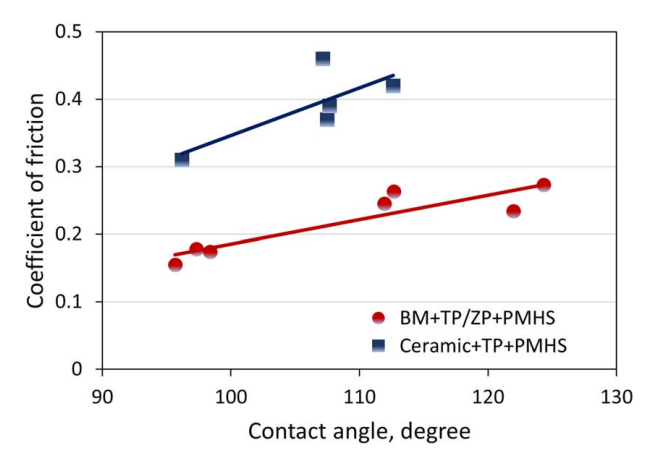


Fig. 10 COF versus CA plot for the coated hydrophobic samples

COF values ranging from 0.234 to 0.273, which were similar to the reference uncoated base materials.

We plotted the COF values of the uncoated and coated BM with the developed coatings against the average roughness in Fig. 9. Besides visualizing the COF of different types of samples, we observed a linear increasing trend of COF with increasing average roughness. This increasing trend was consistent with previous studies with ceramic substrates coated with TP and PMHS [30,34,39] though the relationship between average roughness

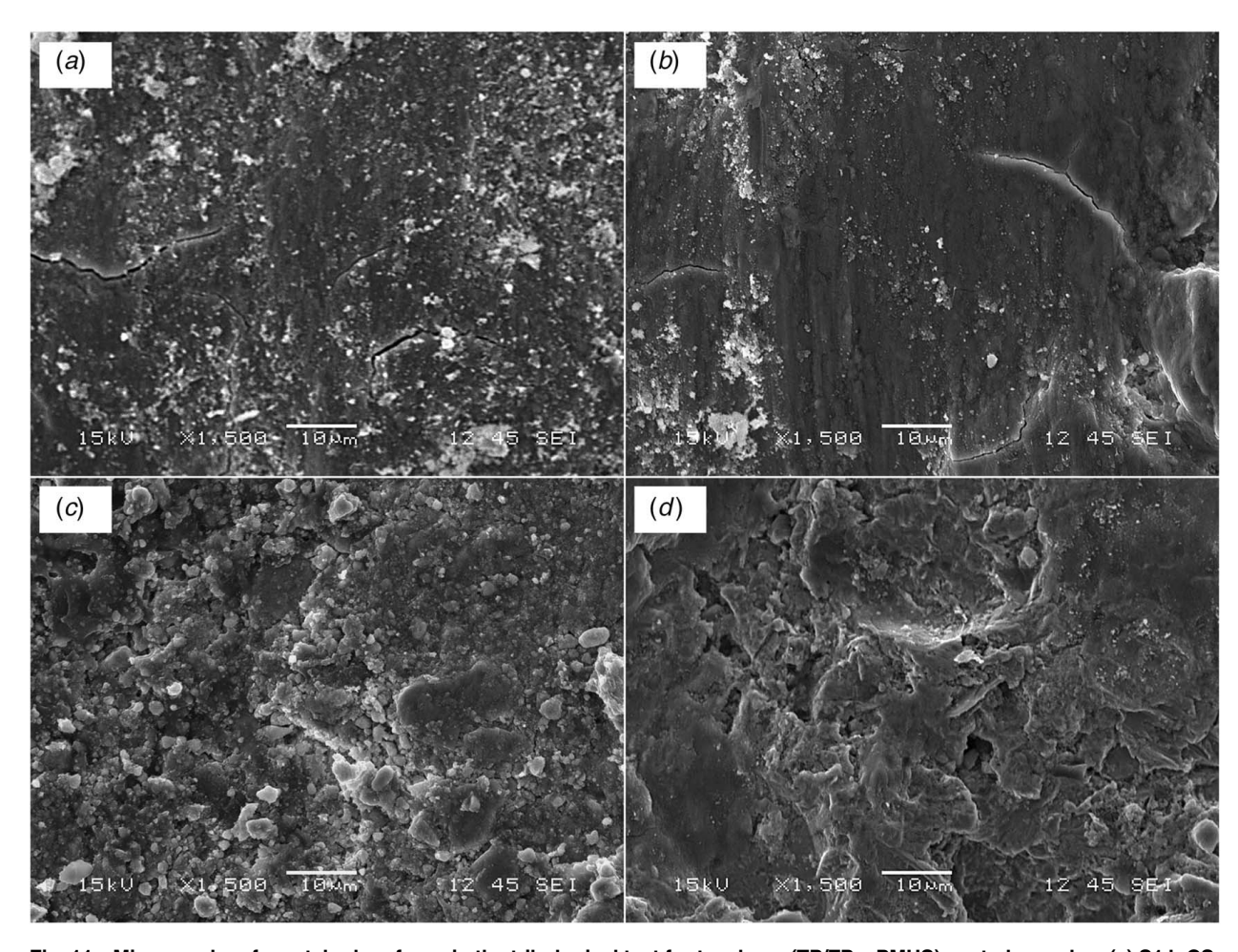


Fig. 11 Micrographs of scratched surfaces in the tribological test for two-layer (TP/ZP + PMHS) coated samples: (a) S1 h CS, (b) S1 h RTP CS, (c) S1 h SS, and (d) S2 h CS

(which is a surface property) and the COF (which is a tribological response) can be more complex [40]. The tribological characterization indicated that the two-layer hydrophobic coatings can be tuned to retain the friction behavior of the base materials while imparting desired hydrophobic properties to the substrate materials.

The COF values of PMHS-coated BM samples and two-layer-coated samples are plotted against the corresponding CAs in Fig. 10. We observed a linear trend, where the COF increased with an increasing CA. This observation was consistent with our previous study using the ceramic tile samples coated with TP and PMHS [34].

We analyzed the SEM micrographs of the scratched two-layer coated surfaces during the tribological tests. The SEM micrographs are shown in Fig. 11. The intensive sliding of the tribometer pin on the coated samples caused visible detaching of the crystalline structures of TP/ZP from the substrates. However, the presence of a thin coating layer on the scratched substrate was clearly visible unlike those observed for the base metals (Fig. 3). In a preliminary observation, the presence of microcracks on the micrographs (Fig. 11) also suggested the retention of the coating layer and abrasion resistance despite the severe sliding. A detailed study involving the wear-rate can reveal more about the durability and abrasion resistance of the coatings.

4 Conclusions

We synthesized TiO_2 - and ZnO-based hydrophilic and hydrophobic surface coatings, applied them to three types of steel substrates, and studied their wetting and tribological properties. The average roughness of the uncoated BM samples ranged between $2.805~\mu m$ and $3.705~\mu m$. The application of the PMHS coating on the BM samples reduced the average roughness values that ranged from $2.039~\mu m$ to $2.071~\mu m$. In contrast, the single coating layer (S1 and S2) notably increased the roughness of the BM samples to the values ranging from $4.004~\mu m$ to $6.473~\mu m$. The samples coated with the two-layer hydrophobic coatings (ZnO/TiO₂-phosphate layer followed by PMHS) exhibited the maximum average roughness values (ranging between $5.016~\mu m$ and $8.805~\mu m$). Here, PMHS effectively amplified the roughness of single-coated substrates. The topological data analysis indicated anisotropic roughness distribution in the coated samples.

The BM samples coated with the two-layer coatings had excellent and stable hydrophobic behavior with CA ranging between 111.93 deg and 124.33 deg. The two-layer S1 CS-PMHS sample had the maximum average roughness and the highest CA. From the tribological characterization, we found that the average COF of the BM samples can range between 0.221 and 0.256. The application of a single layer of hydrophobic PMHS or hydrophilic S1 or S2 coating material reduced the average COF. However, the COF values ranging between 0.234 and 0.273 for the two-layer coated hydrophobic samples reached the levels of the uncoated BM samples. This observation indicated that the developed two-layer hydrophobic coating did not alter the friction behavior of the base materials. Furthermore, the analysis of the scratched surface during the tribological tests revealed some detaching of crystalline structures of ZnO/TiO2-phosphate from the surface.

Acknowledgment

The authors acknowledge the support of the National Science Foundation Rapid (Award No. 2028535).

Conflict of Interest

There are no conflicts of interest.

References

- Bourouiba, L., 2020, "Turbulent Gas Clouds and Respiratory Pathogen Emissions: Potential Implications for Reducing Transmission of COVID-19," JAMA, 323(18), pp. 1837–1838.
- [2] Lewis, D., 2020, "Is the Coronavirus Airborne? Experts Can't Agree," Nature, 580(7802), p. 175.
- [3] Shiu, E. Y., Leung, N. H., and Cowling, B. J., 2019, "Controversy Around Airborne Versus Droplet Transmission of Respiratory Viruses: Implication for Infection Prevention," Curr. Opin. Infect. Dis., 32(4), pp. 372–379.
- [4] Hasan, M. S., Sobolev, K., and Nosonovsky, M., 2021, "Evaporation of Droplets Capable of Bearing Viruses Airborne and on Hydrophobic Surfaces," J. Appl. Phys., 129(2), p. 024703.
- [5] Zhang, S., Diao, M., Yu, W., Pei, L., Lin, Z., and Chen, D., 2020, "Estimation of the Reproductive Number of Novel Coronavirus (COVID-19) and the Probable Outbreak Size on the Diamond Princess Cruise Ship: A Data-Driven Analysis," Int. J. Infect. Dis., 93, pp. 201–204.
- [6] Centers for Disease Control and Prevention (US), 2021, "Science Brief: SARS-CoV-2 and Surface (Fomite) Transmission for Indoor Community Environments," CDC COVID-19 Science Briefs, https://www.cdc.gov/ coronavirus/2019-ncov/more/science-and-research/surface-transmission.html, Accessed August 10, 2021).
- [7] World Health Organization, 2020, "Coronavirus Disease (COVID-19): Cleaning and Disinfecting Surfaces in Non-health Care Settings, https://www.who.int/ news-room/q-a-detail/coronavirus-disease-covid-19-cleaning-and-disinfectingsurfaces-in-non-health-care-settings, Accessed August 10, 2021.
- [8] Cloutier, M., Mantovani, D., and Rosei, F., 2015, "Antibacterial Coatings: Challenges, Perspectives, and Opportunities," Trends Biotechnol., 33(11), pp. 637–652.
- [9] Kaur, R., and Liu, S., 2016, "Antibacterial Surface Design-Contact Kill," Prog. Surf. Sci., 91(3), pp. 136–153.
- [10] Sabbouh, M., Nikitinaa, A., Rogacheva, E., Kraeva, L., Ulasevich, S. A., Skorb, E. V., and Nosonovsky, M., 2021, "Separation of Motions and Vibrational Separation of Fractions for Biocide Brass," Ultrason. Sonochem., 80, p. 105817.
- [11] Heidenau, F., Mittelmeier, W., Detsch, R., Haenle, M., Stenzel, F., Ziegler, G., and Gollwitzer, H., 2005, "A Novel Antibacterial Titania Coating: Metal Ion Toxicity and In vitro Surface Colonization," J. Mater. Sci.: Mater. Med., 16(10), pp. 883–888.
- [12] Botequim, D., Maia, J., Lino, M. M. F., Lopes, L. M. F., Simões, P. N., Ilharco, L. M., and Ferreira, L., 2012, "Nanoparticles and Surfaces Presenting Antifungal, Antibacterial and Antiviral Properties," Langmuir, 28(20), pp. 7646–7656.
- [13] Haldar, J., Weight, A. K., and Klibanov, A. M., 2007, "Preparation, Application and Testing of Permanent Antibacterial and Antiviral Coatings," Nat. Protoc., 2(10), pp. 2412–2417.
- [14] Basak, S., and Packirisamy, G., 2020, "Nano-Based Antiviral Coatings to Combat Viral Infections," Nano-Struct. Nano-Objects, 24(10), p. 100620.
- [15] Faraldos, M., Kropp, R., Anderson, M. A., and Sobolev, K., 2016, "Photocatalytic Hydrophobic Concrete Coatings to Combat Air Pollution," Catal. Today, 259, pp. 228–236.
- [16] Binas, V., Venieri, D., Kotzias, D., and Kiriakidis, G., 2017, "Modified TiO₂ Based Photocatalysts for Improved Air and Health Quality," J. Materiomics, 3(1), pp. 3–16.
- [17] Sano, T., Negishi, N., Koike, K., Takeuchi, K., and Matsuzawa, S., 2004, "Preparation of a Visible Light-Responsive Photocatalyst From a Complex of Ti4+ With a Nitrogen-Containing Ligand," J. Mater. Chem., 14(3), pp. 380–384.
- [18] Ishibai, Y., Sato, J., Akita, S., Nishikawa, T., and Miyagishi, S., 2007, "Photocatalytic Oxidation of NOx by Pt-Modified TiO₂ Under Visible Light Irradiation," J. Photochem. Photobiol. A, 188(1), pp. 106–111.
- [19] Guo, M. Y., Ng, A. M. C., Liu, F., Djurisic, A. B., Chan, W. K., Su, H., and Wong, K. S., 2011, "Effect of Native Defects on Photocatalytic Properties of ZnO," J. Phys. Chem. C, 115(22), pp. 11095–11101.
- [20] Jongnavakit, P., Amornpitoksuk, P., Suwanboon, S., and Ratana, T., 2012, "Surface and Photocatalytic Properties of ZnO Thin Film Prepared by Sol-Gel Method," Thin Solid Films, 520(17), pp. 5561–5567.
- [21] Liu, J., Wang, Y., Ma, J., Peng, Y., and Wang, A., 2019, "A Review on Bidirectional Analogies Between the Photocatalysis and Antibacterial Properties of ZnO," J. Alloys Compd., 783, pp. 898–918.
- [22] Bhushan, B., Nosonovsky, M., and Jung, Y., 2008, Nanotribology and Nanomechanics, B. Bhushan, ed., Springer, Berlin/Heidelberg.
- [23] Paven, M., Mammen, L., and Vollmer, D., 2016, Smart Materials for Advanced Environmental Applications, P. Wang, ed., The Royal Society of Chemistry, London, pp. 209–243.
- [24] Feng, X., and Jiang, L., 2006, "Design and Creation of Superwetting/Antiwetting Surfaces," Adv. Mater., 18(23), pp. 3063–3078.
- [25] Lafuma, A., and Quéré, D., 2003, "Superhydrophobic States," Nat. Mater., 2(7), pp. 457–460.
- [26] Flores-Vivian, I., Hejazi, V., Kozhukhova, M. I., Nosonovsky, M., and Sobolev, K., 2013, "Self-assembling Particle-Siloxane Coatings for Superhydrophobic Concrete" ACS Appl. Mater. Interfaces, 5(24), pp. 13284–13294.
- Concrete," ACS Appl. Mater. Interfaces, 5(24), pp. 13284–13294.

 [27] Yao, K. X., and Zeng, H. C., 2008, "Fabrication and Surface Properties of Composite Films of SAM/Pt/ZnO/SiO2," Langmuir, 24(24), pp. 14234–14244.
- [28] Arabzadeh, A., Ceylan, H., Kim, S., Gopalakrishnan, K., and Sassani, A., 2016, "Superhydrophobic Coatings on Asphalt Concrete Surfaces," Transp. Res. Rec., 2551(1), pp. 10–17.
- [29] Sobolev, K., and Batrakov, V. G., 2007, "Effect of a Polyethylhydrosiloxane Admixture on the Durability of Concrete With Supplementary Cementitious Materials," J. Mater. Civil Eng., 19(10), pp. 809–813.

- [30] Lanka, S., Alexandrova, E., Kozhukhova, M., Hasan, M. S., Nosonovsky, M., and Sobolev, K., 2019, "Tribological and Wetting Properties of TiO₂ Based Hydrophobic Coatings for Ceramics," ASME J. Tribol., 141(10), p. 101301.
- [31] Hasan, M. S., Kordijazi, A., Rohatgi, P. K., and Nosonovsky, M., 2022, "Triboinformatics Approach for Friction and Wear Prediction of Al-Graphite Composites Using Machine Learning Methods," ASME J. Tribol., 144(1), p. 011701
- [32] Hasan, M. S., Kordijazi, A., Rohatgi, P. K., and Nosonovsky, M., 2021, "Triboinformatic Modeling of Dry Friction and Wear of Aluminum Base Alloys Using Machine Learning Algorithms," Tribol. Int., 161, p. 107065.
- [33] Bowden, F. P., and Tabor, D., 1950, Friction Lubrication of Solids, Part 1, Clarendon, London.
- [34] Hasan, M. S., and Nosonovsky, M., 2020, "Lotus Effect and Friction: Does Nonsticky Mean Slippery?," Biomimetics, 5(2), p. 28.

- [35] Hasan, M. S., Kordijazi, A., Rohatgi, P. K., and Nosonovsky, M., 2022, "Machine Learning Models of the Transition From Solid to Liquid Lubricated Friction and Wear in Aluminum-Graphite Composites," Tribol. Int., 165, p. 107326.
- [36] Hasan, M. S., and Nosonovsky, M., 2021, "Topological Data Analysis for Friction Modeling," Europhys. Lett., 135(2021), p. 56001.
- [37] Zhukov, M., Hasan, M. S., Nexterov, P., Sabboukh, M., Burdulenko, O., Skorb, E. V., and Nosonovsky, M., 2021, "Topological Data Analysis of Nanoscale Roughness in Brass Samples," ACS Appl. Mater. Interfaces, 14(1), pp. 2351–2359.
- [38] Wang, X., and Zhang, Q., 2020, "Insight Into the Influence of Surface Roughness on the Wettability of Apatite and Dolomite," Minerals, 10(2), p. 114.
- [39] Uesugi, M., and Kishida, H., 1986, "Frictional Resistance at Yield Between Dry Sand and Mild Steel," Soils Found., 26(4), pp. 139–149.
- [40] Menezes, P. L., and Kailas, S. V., 2016, "Role of Surface Texture and Roughness Parameters on Friction and Transfer Film Formation When UHMWPE Sliding Against Steel," Biosurf. Biotribol., 2(1), pp. 1–10.